Marine Geology 438 (2021) 106526

Contents lists available at ScienceDirect

Marine Geology

journal homepage: www.elsevier.com/locate/margo

Research Article

Using a transect-focused approach to interpret satellite images and analyze shoreline evolution in Haiyang Beach, China

Xiaodong Zhang *, Xiawei Tan, Rijun Hu *, Longhai Zhu, Chuang Wu, Zuosheng Yang

Key Lab of Submarine Geosciences and Prospecting Techniques, MOE and College of Marine Geosciences, Ocean University of China, Qingdao 266100, China

ARTICLE INFO

Editor: Edward Anthony

Keywords:
Satellite image
Shoreline evolution
Beach transect
Shoreline indicator
Beach profile shape
Coastal engineering

ABSTRACT

This paper devises a set of simple and practical method for interpreting hundreds of free medium-resolution satellite images to study beach evolution. The method focuses on beach transects, integrates the computer-aided and subpixel recognition technologies, and derives multiple shoreline indicators and historical beach profile shape. This paper also introduces how to use the method with a case study. The case study uses 880 Landsat images from 1984 to 2020 to examine the historical evolution of the complex Haiyang Beach in China as well as its responses to onshore and offshore engineering projects.

The results not only show the detailed temporal and spatial changes of the upper beach based on dry/wet and high-water lines, but also the changes of the middle and lower beach based on mean-water, low-water, and low boundary lines, as well as the changes of beach profile shape, beach slope, and intertidal width. The random errors of the dry/wet, high-water, mean-water, and low-water lines are 7.8 m, 10.5 m, 15.9 m, and 19.2 m, respectively. The random errors not only result from the geo-reference process of satellite images and the recognition process of shoreline positions, but are also affected by random water level fluctuations and irregular undulations of the beach profile. This paper also discusses the similarities, differences, and applicability of these shoreline indicators. It is found that the evolution of dry/wet and high-water lines are similar and mainly affected by onshore engineering projects while the evolution of mean-water, low-water, and low boundary lines are similar and mainly affected by offshore engineering projects.

The method provided in this paper can comprehensively evaluate beach evolution based on free satellite images, and would be helpful for understanding and protection of the beaches affected by intensified or intensifying engineering projects and human activities.

1. Introduction

Beaches have multiple functions, such as coastal tourism, storm protection, and water purification (Alexandrakis et al., 2015; López et al., 2016; Burvingt et al., 2017; Ballesteros et al., 2018; You et al., 2018; Jackson and Nordstrom, 2020). In recent decades, under the influence of intensified human activities, drastic reduction in river sediment discharged into the sea, and rapid sea level rise, 24–70% of global beaches have suffered erosion (Bird, 1985; Nicholls and Cazenave, 2010; Cazenave and Cozannet, 2014; Ranasinghe, 2016; Luijendijk et al., 2018; Burt and Bartholomew, 2019; Jackson and Nordstrom, 2020; Vousdoukas et al., 2020a). Vousdoukas et al. (2020a, 2020b) predicted that half of the world's beaches may disappear by the end of this century. Although the above predication is still controversial, it is undeniable that beach erosion is attracting worldwide attention and concern (Brooks, 2020; Cooper et al., 2020).

China's coastal areas are densely populated and the most vulnerable areas in the world to coastal erosion (Cai et al., 2009; Nicholls and Cazenave, 2010). Previous studies show that approximately 70% of China's beaches have been eroded, with an erosion rate of approximately 1–3 m/year (Zhuang et al., 1989; Xia et al., 1993; Cai et al., 2009; Li et al., 2013; Zhang et al., 2019). With the rapid economic development in recent decades, various coastal engineering projects have appeared along the coast of China, with dozens of offshore artificial islands alone. A higher proportion of eroded beaches, coupled with the recent intensification of human activities, makes the evolution of China's beaches even more worrying.

Field survey data are comprehensive and usually used in beach evolution studies; however, long-term and frequently measured data are only available on a limited number of beaches (e.g., Turner et al., 2016;

* Corresponding authors.
E-mail addresses: zxd@ouc.edu.cn (X. Zhang), hrj@ouc.edu.cn (R. Hu).

https://doi.org/10.1016/j.margeo.2021.106526
Received 20 January 2021; Received in revised form 25 May 2021; Accepted 31 May 2021
Available online 6 June 2021
0025-3227/© 2021 Elsevier B.V. All rights reserved.

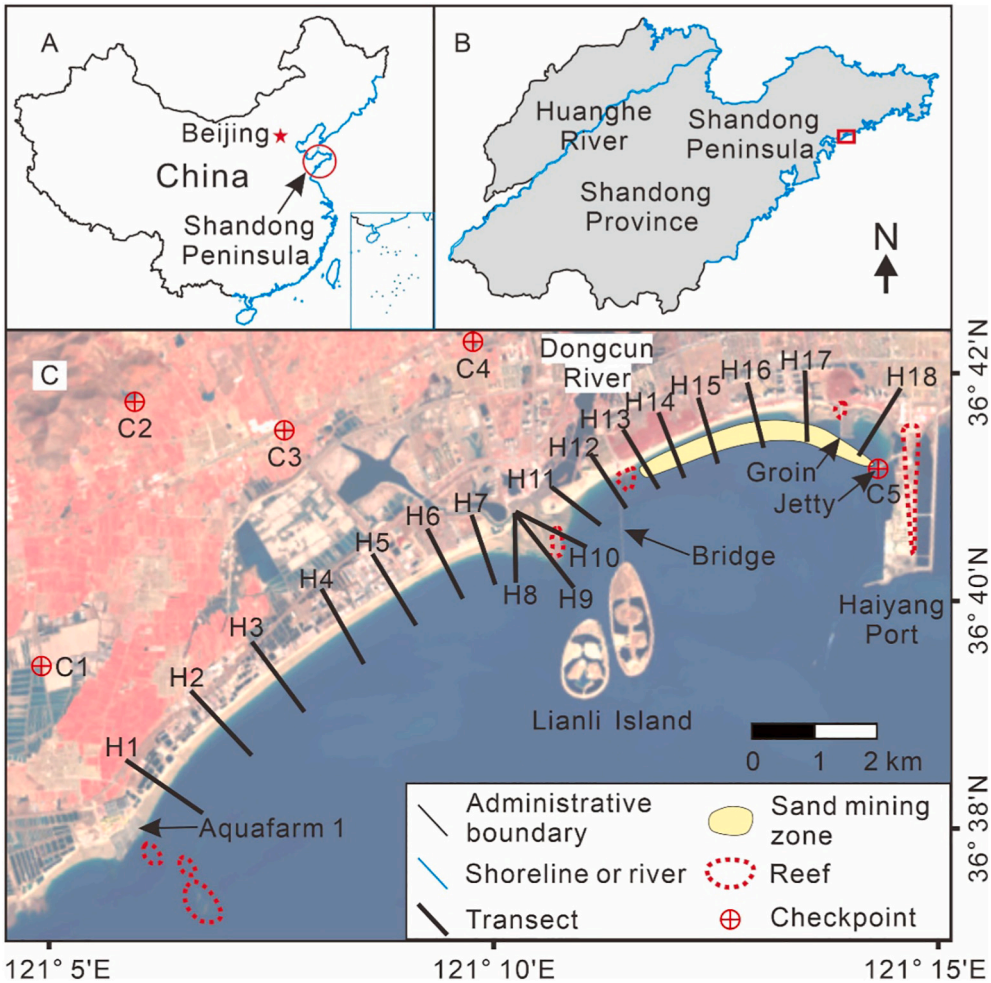

Fig. 1. Location of Haiyang Beach in China (A), Shandong Province (B), and the study transects along Haiyang Beach (C). The background of Fig. C is a recent standard false-color Landsat image.

Wenneker et al., 2016; Ludka et al., 2019). Satellite images have the advantages of wide coverage and short revisit periods. Many studies have used long-term and freely available medium-resolution satellite images to evaluate the evolution of deltas and tidal flats with large widths (hundreds to thousands of meters) and change rates (several to tens of meters per year) (e.g., Rouse et al., 1978; Ryu et al., 2002; Couvillion et al., 2011; Anthony, 2015; Brown and Nicholls, 2015; Zhang et al., 2019, 2020). There are also many studies using satellite images to evaluate the evolution of beaches (e.g., Webb and Kench, 2010; Romine and Fletcher, 2012; Luijendijk et al., 2018; Mentaschi et al., 2018; Segura et al., 2018; Zhang et al., 2019; Vousdoukas et al., 2020a). However, in theory, the use of medium-resolution (~30 m) satellite images to study the evolution of beaches with small widths (commonly less than 200 m) and change rates (less than several meters per year), is limited in accuracy (Pardo-Pascual et al., 2012; Hagenaars et al., 2018).

Pardo-Pascual et al. (2012, 2018) used subpixel technology to calibrate satellite images and extract shorelines, and the standard deviations of shoreline positions interpreted from the satellite images, which had resolutions of 10–30 m, was decreased to 4.7–6.7 m. García-Rubio et al. (2015) searched the subpixel positions of shoreline using spatial smoothing method, and a standard deviation of 1.37 m over 8 km of shoreline was reached on satellite images with resolutions of 10 m. Vos et al. (2019) combined supervised image classification algorithm and subpixel contouring algorithm to extract shorelines of five beaches, and the standard deviations of shoreline positions interpreted from Sentinel and Landsat images, which had resolutions of 10–30 m, varied between 7.3 and 12.7 m. Although the sub-pixel technology greatly reduces the shoreline position error, it is still relatively large for studying the evolution of beaches.

Maiti (2009), Almonacid-Caballer et al. (2016), Hagenaars et al. (2018), and Zhang et al. (2018a, 2019) recommend using dozens to hundreds of satellite images and statistical methods in the study of shoreline evolution to obtain reliable results. The use of dozens to hundreds of satellite images not only helps to derive accurate shoreline change rates through statistics, but also helps to obtain the detailed and

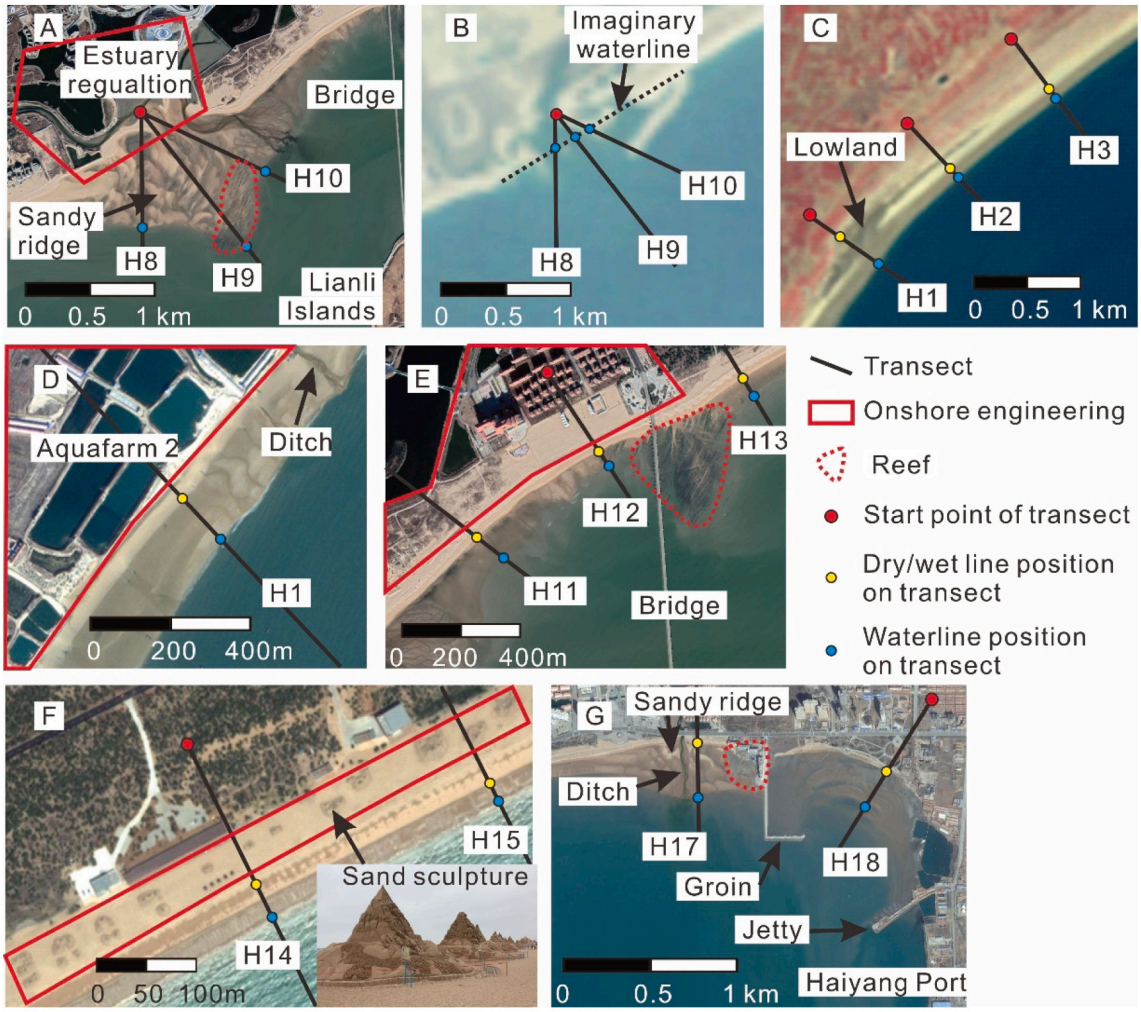

Fig. 2. Geomorphological features and coastal engineering projects of Haiyang Beach. (A) the Dongcun River delta at low tide, (B) the funnel-shaped Dongcun River mouth at high tide, (C) lowland by transect H1, (D) aquafarms and ditch by H1, (E) onshore land reclamation by H11–12, (F) sand sculptures by H14–16, (G) ditch, sandy ridges, reef, groin, jetty and Haiyang Port by H17–18. The backgrounds of Figs. B—C are Landsat images, and the backgrounds of Figs. A, D-G are high-resolution satellite images from Google Earth.

long-term beach evolution history. Using subpixel shoreline recognition technology to interpret as many satellite images as possible will be the developmental direction of beach evolution research.

Previous methods first identify the shorelines on satellite images, and then calculate the shoreline positions on study transects, which are mostly perpendicular to local shorelines, using the popular DSAS software (an ArcGIS extension programmed by Thieler et al., 2009) or self-programmed software (Luijendijk et al., 2018; Mentaschi et al., 2018; Vos et al., 2019; Vousdoukas et al., 2020a). Before the long time-sequence shoreline positions on transect are available to study beach evolution, all shorelines on all images must be identified. Zhang et al. (2018a, 2018b, 2018c, 2019, 2020) propose to directly recognize the shoreline positions on study transects using a transect-focused and computer-aided shoreline position recognition software (CASPRS). Focusing on the study transects and only identifying the shoreline positions on the transects, the method avoids interpreting all the shorelines on all images. Therefore, the method can save a lot of time, mainly the time required to manually check and correct the shorelines, which is conducive to processing as many satellite images as possible. In addition, previous subpixel shoreline recognition methods mainly focused on automatic recognition algorithms, and paid less attention to later corrections. As a result, they can only process good-quality images with less than 10% cloud cover and uninfluenced by intertidal bars, shoals and troughs (e.g., Vos et al., 2019), which is not conducive to using as many satellite images as possible to further improve the accuracy of shoreline change.

Previous beach evolution studies solely used the high-water line (Vos et al., 2019; Zhang et al., 2019), low-water line (Romine and Fletcher, 2012), dry/wet line (Pagán et al., 2016, 2017, 2018), waterline (Pardo-Pascual et al., 2018), or the shoreline derived from moving average composite image (Luijendijk et al., 2018; Vousdoukas et al., 2020a). Comprehensive beach evolution studies based on multiple shoreline

Table 1
Main onshore and offshore engineering projects by Haiyang Beach.

Project name	Alongshore position (transect No.)	Cross-shore position (onshore and/or offshore)	Length (alongshore) (km)	Width (cross-shore)(km)	Project area (km^2)	Construction/ implementation time (year)
Aquafarm 1	H1	Onshore	0.6	0.3	0.2	2006
Aquafarm 2	H1	Onshore	0.7	0.4	0.1	2007
Estuary regulation	H8–10	Onshore	0.8	1	0.8	2003
Land reclamation	H11–12	Onshore	1	0.5	0.5	2002
Sand sculptures	H14–15	Onshore	0.6	0.05	/	2006
Groin	H17	Onshore and offshore	/	0.6	/	1976
Jetty	H18	Onshore and offshore	/	0.6	/	1976
Haiyang Port	H18	Onshore and offshore	0.7	2.4	1.8	1976
Lianli Island	H8–10	Offshore	2	1.7	1.5	2010
Bridge	H12	Onshore and Offshore	/	1.5	/	2010
Sand mining	H13–18	Offshore	4	0.5	2.0	2006

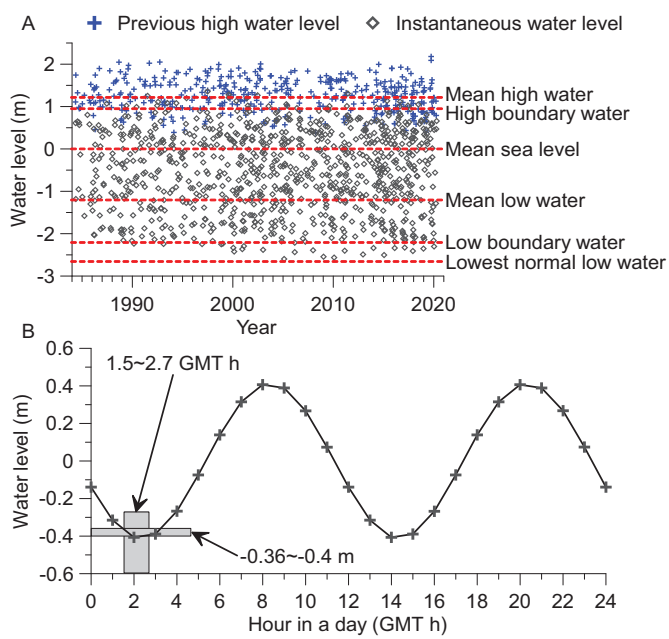

Fig. 3. Previous high water levels before Landsat images were taken and instantaneous water levels when Landsat images were taken (A) and hourly mean water levels (B).

indicators have not been reported. Moreover, previous studies mainly calculated the average beach slope (e.g., Vos et al., 2020), without considering the slope difference between the upper and lower beaches (e.g., Turner et al., 2016). The studies on the entire beach profile shape based on satellite images have also not been reported.

In this paper, we integrated the subpixel shoreline recognition technology and revised the CARPRS software to make it suitable for studying the evolution of beaches, and used the revised CARPRS software and 880 Landsat satellite images from 1984 to 2020, employing 18 study transects (H1–18, Fig. 1) and multiple shoreline indicators to comprehensively study the evolution of Haiyang Beach, a complex beach that is composed of many geomorphic units and has been seriously affected by onshore and offshore engineering projects. The purpose is to evaluate the application potential of the transect-focused software and method in beach evolution study and the responses of multiple shoreline indicators to onshore and offshore engineering projects.

2. Study area

Haiyang Beach is located in Shandong Province, China (Fig. 1). The beach, 15 km long and 50–700 m width, is the most famous tourist attraction in Haiyang City. The Dongcun River enters the sea in the middle of Haiyang Beach, forming the Dongcun River delta, which appears at low tide but is submerged at high tide (Fig. 2A, B). In 2003, the sand ridges on both sides of the Dongcun River mouth were dredged, resulting in the current river mouth looking like a funnel at high tide (Fig. 2B). There is a lowland area around H1 (Fig. 2C), and the lowland remained moist year-round until it was gradually enclosed for aquacultural use (Fig. 2D).

There are many engineering projects around Haiyang Beach including the aquafarms 1 and 2 by transects H1 (Fig. 1C, Fig. 2D), the estuary regulation project by transects H8–10 (Fig. 2A, B), the land reclamation project by transects H11–12 (Fig. 2E), the sand sculptures by transects H14–15 (Fig. 2F), a groin, a jetty and the Haiyang Port by transects H17–18 (Fig. 2G), two offshore artificial islands, together referred to as Lianli Island (in Chinese, Lianli means couple in love), and a bridge connecting Lianli Island to the mainland (Fig. 1C)(Table 1). To build the sand sculptures, sand was mined in the surrounding offshore water less than 1 km from the shore and less than 5 m in depth (Fig. 1C) because the sediment on the seafloor farther out to sea is mainly composed of silt (Zhang et al., 2012; Ren et al., 2016). The naturally formed delta, native reefs, and manmade engineering divide Haiyang Beach into two slightly arc-shaped beaches (the beaches around transects H1–7 and H11–18, Fig. 1C).

Haiyang Beach is mainly composed of well-sorted medium and fine sand (the median size is −0.67-2.72 φ with an average of 1.43 φ), the Dongcun River delta and the beach between the northern groin and jetty are mainly composed of sand and silt, and the offshore area is mainly composed of silt and silty clay (the median size is 5–7 φ with an average of 5.58 φ) (Zhang et al., 2012; Ren et al., 2016).

The tide at Haiyang Beach is a normal semidiurnal tide with a medium tidal range. Compared with the 1985 national elevation benchmarks, the mean high water is 1.21 m, the mean sea level is 0 m, the mean low water is −1.20 m, and the lowest normal low water is −2.67 m (Fig. 3A) (Editorial Board of China Bay Survey, 1993). The waves in the

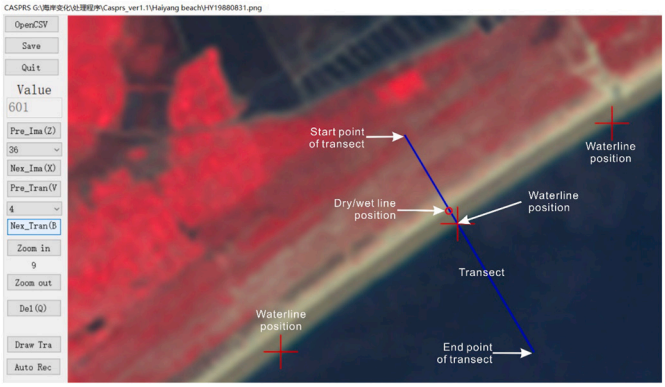

Fig. 4. Operation interface of computer-aided shoreline position recognition software (CASPRS).

study area mainly come from the southwest, and the year-round hydrological observation data at the station 12 km northeast of the study area show that 96% of the waves are less than 1 m in height. The net transport direction of nearshore sediment is to the northeast, and the alongshore sediment transport rate is 0.16–0.19 M m^3/year (Zhang et al., 2012; Ren et al., 2016).

The sea level along the coast of China is rising at a rate of 3.4 mm/year (China Sea Level Bulletin 2019, http://www.mnr.gov.cn/). However, the crust of eastern Shandong Province is also rising at a rate of 2–3 mm/year (Li et al., 2001), which offsets most of the impact of sea level rise. Therefore, the impact of sea level rise on Haiyang Beach is small and will not be discussed.

3. Data and methods

3.1. Data source and preprocessing of satellite images

A total of 880 Landsat satellite images from 1984 to 2020 were used in this study. The dataset was provided by the Earth Resources Observation and Science Center (http://glovis.usgs.gov). The resolution of the images is 30 m, and the geo-reference error is less than 0.4 pixels (12 m) (http://glovis.usgs.gov). All the Landsat TM, ETM+, and OLI images that could display at least half of Haiyang Beach were downloaded. Haiyang Beach is covered by two paths (119 and 120) of the Landsat satellites, so the number of downloaded images is twice that of the area covered by a single path. The images were synthesized using a standard false-color method, which combines near infrared, red, and green bands into red, green, and blue images. Finally, the images of Haiyang Beach were cropped from the synthesized false-color images, and the width and height of the cropped images are 503 pixels (15.06 km) and 325 pixels (9.72 km), respectively (Fig. 1C).

3.2. Recognition of waterline, dry/wet line, and checkpoint

Eighteen transects and six shoreline indicators known as waterline, dry/wet line, high-water line, mean-water line, low-water line, and low boundary line were used to quantitatively study the historical evolution of Haiyang Beach (Fig. 1C, 2). The waterline and dry/wet line are directly identified from the satellite images, and the high-water, mean-water, low-water, and low boundary lines are derived from the waterline. In the Dongcun River delta, dry sand ridges are scattered on the wet beach (Fig. 2A), therefore, the dry/wet line positions on H8–10 were not identified.

The subpixel shoreline recognition technology is integrated into the transect-focused CASPRS software. From the start point to the end point of each transect, CASPRS sets an interpolation point every 1 m and uses the bilinear interpolation method to calculate the color value of each interpolation point according to adjacent 4 pixels. Then, CASPRS uses 120 adjacent interpolation points to calculate the Normalized Difference Water Index (NDWI) gradient of the middle interpolation point, and the point with the largest gradient is used as the reference position of the waterline on the transect. The overall automatic identification time is about one minute.

To facilitate the corrections, we have designed a convenient human-computer interaction interface (Fig. 4). Users can switch between different images and transects, zoom the image by clicking the buttons or pressing the keyboard. Users can correct the automatic recognition result by clicking the actual shoreline position on the image or delete it by clicking the "Del" button. Using CASPRS, the manual correction of a shoreline position on a transect can be fulfilled in a second. Therefore, the overall correction time of the shoreline positions on the 18 transects of 880 images is within 5 h. Users can also draw a scatter graph according to the automatic identification results and select the outliers to correct. In this way, the overall correction time will be less.

The dry/wet line positions were completely manually identified using the CARPRS software, because its automatic recognition algorithm has not been designed yet. For two reasons: (1) reduce the workload and (2) the variation range of dry/wet line positions is small, and according to the recognition results of waterlines, the images with low data acquisition ratios were eliminated, leaving a total of 411 images for use in identifying the dry/wet line positions on the transects. The manual recognition time of the dry/wet lines is also about 1 s per transect per image, and the overall recognition time of all the dry/wet line positions on 15 transects of the 411 images is within 2 h.

Five checkpoints C1–5 were used to assess the recognition error of CASPRS (Fig. 1C). These 5 checkpoints were corners or intersections of

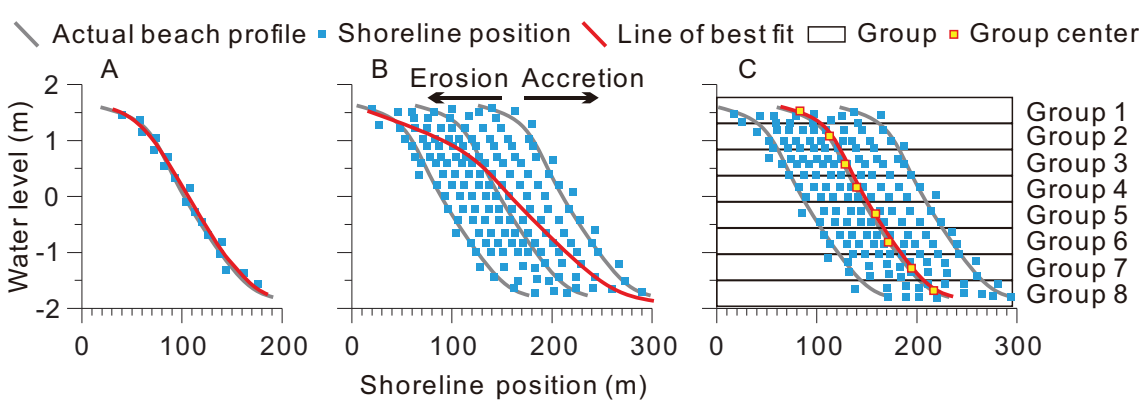

Fig. 5. Calculation methods of beach profile shape. (A) Simple regression analysis when the beach profile is static, (B) incorrect beach profile shape derived from simple regression analysis when the beach profile is dynamic, and (C) group regression analysis when the beach profile is dynamic.

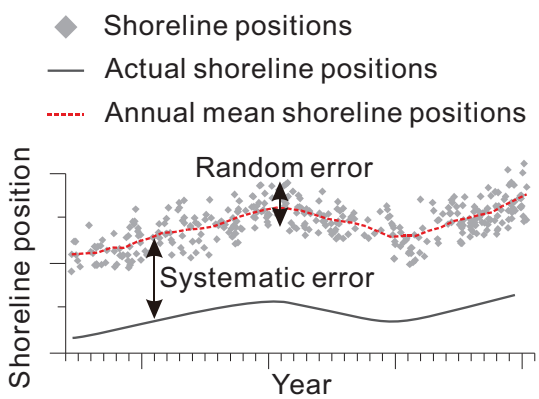

Fig. 6. The systematic and random errors of shoreline position.

man-made buildings that existed throughout the study period and have not changed significantly. For each checkpoint, two transects were set along the X and Y directions of the image, and then CASPRS was used to manually identify the positions of the checkpoints on the two transects. The images used to identify the checkpoints are also the aforementioned 411 images.

3.3. Postprocess of the shoreline positions

The dry/wet line moves slightly on the upper beach since it is mainly affected by the previous high water, and the waterline moves greatly on the whole beach with the instantaneous water (Boak and Turner, 2005; Pagán et al., 2016; Zhang et al., 2018a). Therefore, it is necessary to know the historical high and instantaneous water levels. NAO.99b (Matsumoto et al., 2000), a tide simulation model that is specially optimized for East Asian waters, was used to calculate simulated hourly water levels. The simulated hourly water levels were further used to calculate the previous high water levels before the satellite images were taken and the instantaneous water levels when the satellite images were taken.

When the beach profile is static, simple regression analysis of the water levels and shoreline positions can be used to derive the beach profile shape (Fig. 5A). However, when the beach profile moves landward/seaward due to erosion/accretion, the beach profile shape derived from the simple regression analysis is incorrect (Fig. 5B, Vos et al., 2020). Differing from the method based on frequency domain analysis and linear assumption (Vos et al., 2020), the group regression analysis method, a simple and commonly used method when the variables used in regression analysis have large random errors, was used to calculate the beach profile shape (Fig. 5C). The shoreline positions were first grouped, then their group centers were calculated, and finally, the

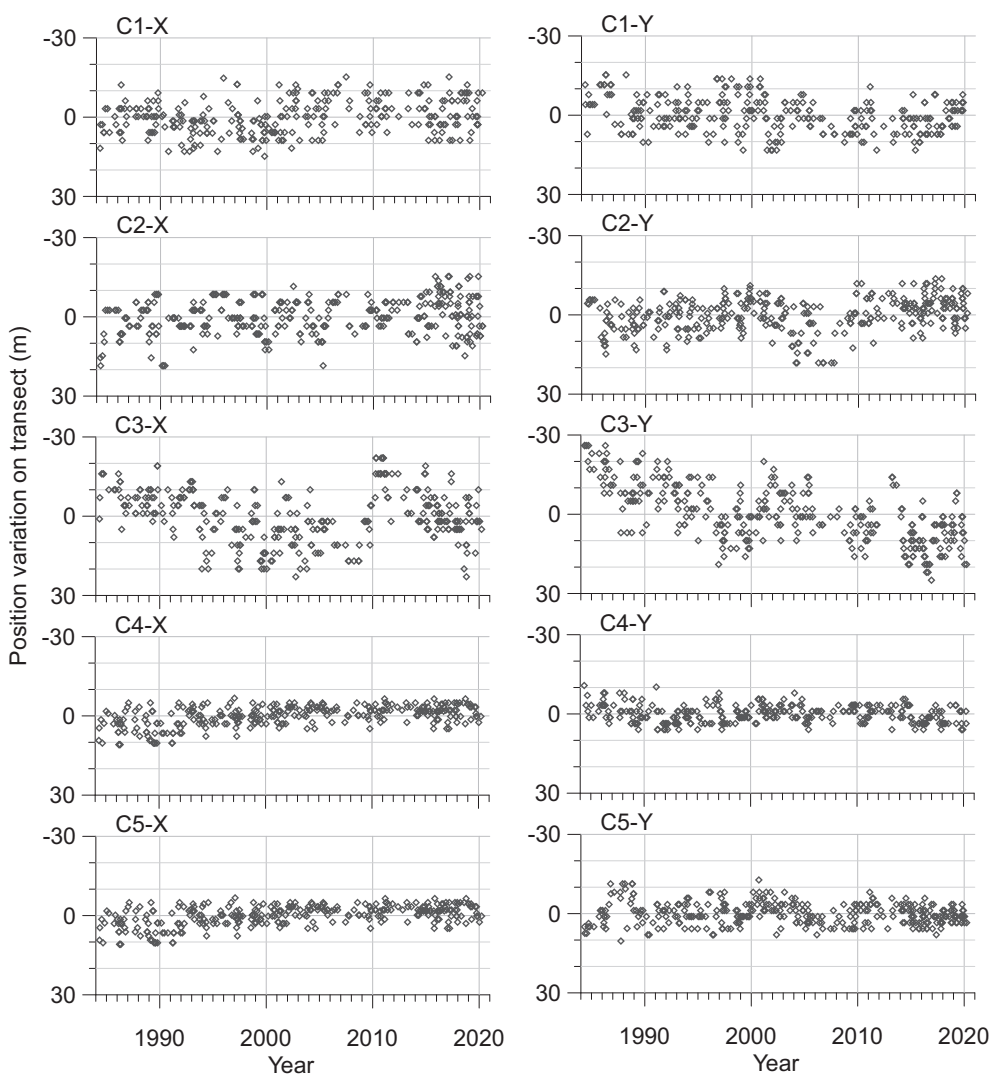

Fig. 7. Position variations of checkpoints C1–5 on the transects of X (east-west) and Y (north-south) directions.

Table 2
Error statistics of the positions of the checkpoints C1–5 in the east-west (X) and north-south (Y) directions.

Checkpoint	Direction	Number of images	Data acquired	Data acquisition ratio	Standard deviation (m)
C1	X	411	291	71%	6.4
	Y	411	292	71%	6.4
C2	X	411	365	89%	6.5
	Y	411	356	87%	6.3
C3	X	411	333	81%	9.7
	Y	411	330	80%	10.8
C4	X	411	308	75%	3.8
	Y	411	320	78%	3.3
C5	X	411	333	81%	6.4
	Y	411	339	82%	4.2
Average		411	327	79%	6.4

simple regression analysis was performed using the group centers.

The positions of the high-, mean-, and low-water lines were calculated according to Eqs. 1–3 revised after Zhang et al. (2019), respectively:

$$P_{high} = P_{waterline} - (WL_{high} - WL)/S_{high}, \text{ when the water level is} > 0.3 \text{ m} \quad (1)$$

$$P_{mean} = P_{waterline} - (WL_{mean} - WL)/S_{mean}, \text{ when the water level is} - 1\text{–}0.5 \text{ m} \quad (2)$$

$$P_{low} = P_{waterline} - (WL_{low} - WL)/S_{low}, \text{ when the water level is} < 0 \text{ m} \quad (3)$$

where P_{high}, P_{mean}, P_{low}, and $P_{waterline}$ are the positions of high-, mean-, low-water lines, and waterline on the transect, respectively; WL, WL_{high}, WL_{mean}, and WL_{low} are instantaneous water level, mean high water, mean sea level, and mean low water, respectively; and S_{high}, S_{mean}, and S_{low} are the slopes when the water level is >0.3 m, −1–0.5 m, and < 0 m, respectively. The reason for not using all the waterline position data but using the data when the water level is >0.3 m to calculate the P_{high} is to minimize the additional error introduced by the nonlinear change of the beach profile. The reasoning is the same for the calculation of P_{mean} and P_{low}.

The annual mean P_{high}, P_{mean}, and P_{low} were further derived, and the erosion rates were calculated using linear regression analysis of the annual mean values (Almonacid-Caballer et al., 2016). The intertidal width was defined as the difference between the annual mean P_{high} and P_{low} (Zhang et al., 2019).

3.4. Error assessment method

For the error evaluation of the shoreline position, there are two aspects: the systematic error (or non-zero mean) and the random error (or variation range) (Fig. 6). To the assessment of systematic error, the shoreline position should be compared with the higher-accuracy result obtained during the same period. However, the persistency of the systematic error ensures that its effects on beach evolution study are limited (Luijendijk et al., 2018). Therefore, the systematic error of shoreline position was not assessed in this paper. To the assessment of random error, if the shoreline position remains unchanged, the random error will be equivalent to the standard deviation derived from Eq. 4. However, since the shoreline changes position both in long and short periods, the standard deviation includes not only the random error but also the long- and short-term trends of the shoreline position. To overcome the effect of the long-term shoreline change, this paper uses Eq. 5, which replaces the overall mean value in Eq. 4 with the annual mean shoreline positions to calculate the modified standard deviation. Although the long-term shoreline change trends can be mostly eliminated by using the annual mean shoreline positions, the short-term shoreline change, such as the seasonal shoreline change, still exist. Therefore, the random error derived from Eq. 5 will be slightly larger than the actual random error, and a concrete error assessment based on the actual shoreline positions measured at the satellite image procurement times is still needed to be carried out. The random error of the checkpoint position is evaluated using Eq. 4 since the checkpoint position remained basically unchanged in the study period.

$$\text{Random error}_{checkpoint} = \text{standard deviation} = \sqrt{\frac{1}{n-1}\sum_{i=1}^{n}(x_i - \overline{x})^2} \quad (4)$$

$$\text{Random error}_{shoreline\ position} = \text{modified standard deviation} = \sqrt{\frac{1}{n-1}\sum_{i=1}^{n}(x_i - \overline{x_y})^2} \quad (5)$$

where n is the total number of data, i is the serial number, x_i is the i-th data, $\overline{x}$ is the overall mean value, and $\overline{x_y}$ is the annual mean value in the y-th year.

4. Results

4.1. Historical water levels

The previous high water levels before the Landsat images were taken fluctuated around the mean high water, however, the instantaneous water levels when the Landsat images were taken rarely exceeded the mean high water (Fig. 3A). The high and low boundary waters, which are defined as the average of the maximum and minimum instantaneous water levels in a year, respectively, are used to quantitatively indicate the above abnormalities. The high boundary water was 0.98 m, which was lower than the mean high water, and the low boundary water was −2.19 m, which was close to the lowest normal low water level (Fig. 3A).

Using all the simulated hourly water levels of Haiyang Beach from 1984 to 2020, the hourly mean water levels in a day were obtained (Fig. 3B). The results show that the water levels were low at 2 and 14 GMT h but high at 8 and 20 GMT h, and the difference between the low and high water levels was as high as 0.8 m, which is mainly caused by the influence of the S2 tidal component (the second-strongest component, with a period of 12 h). In the shooting times of the Landsat TM, ETM+, and OLI images of the study area, which were 1.5–2.7 GMT h (local 9.5–10.7 a.m.), the hourly mean water levels were − 0.36 ~ −0.4 m, exactly the minimum value in a day. The above explains why the instantaneous water levels were relatively low.

4.2. Positions of checkpoints C1–5

The positions of checkpoints C1–5 fluctuate on the X and Y directions (Fig. 7), and the error analyses are shown in Table 2. The position variation of C3 is relatively large, and the random errors are 9.7 m and 10.8 m in the X and Y directions, respectively. C3 is located at the intersection of roads, and its larger errors compared with other checkpoints may be related to the maintenance of the roads and the seasonal change of the trees along the roads. In general, the positions of these 5

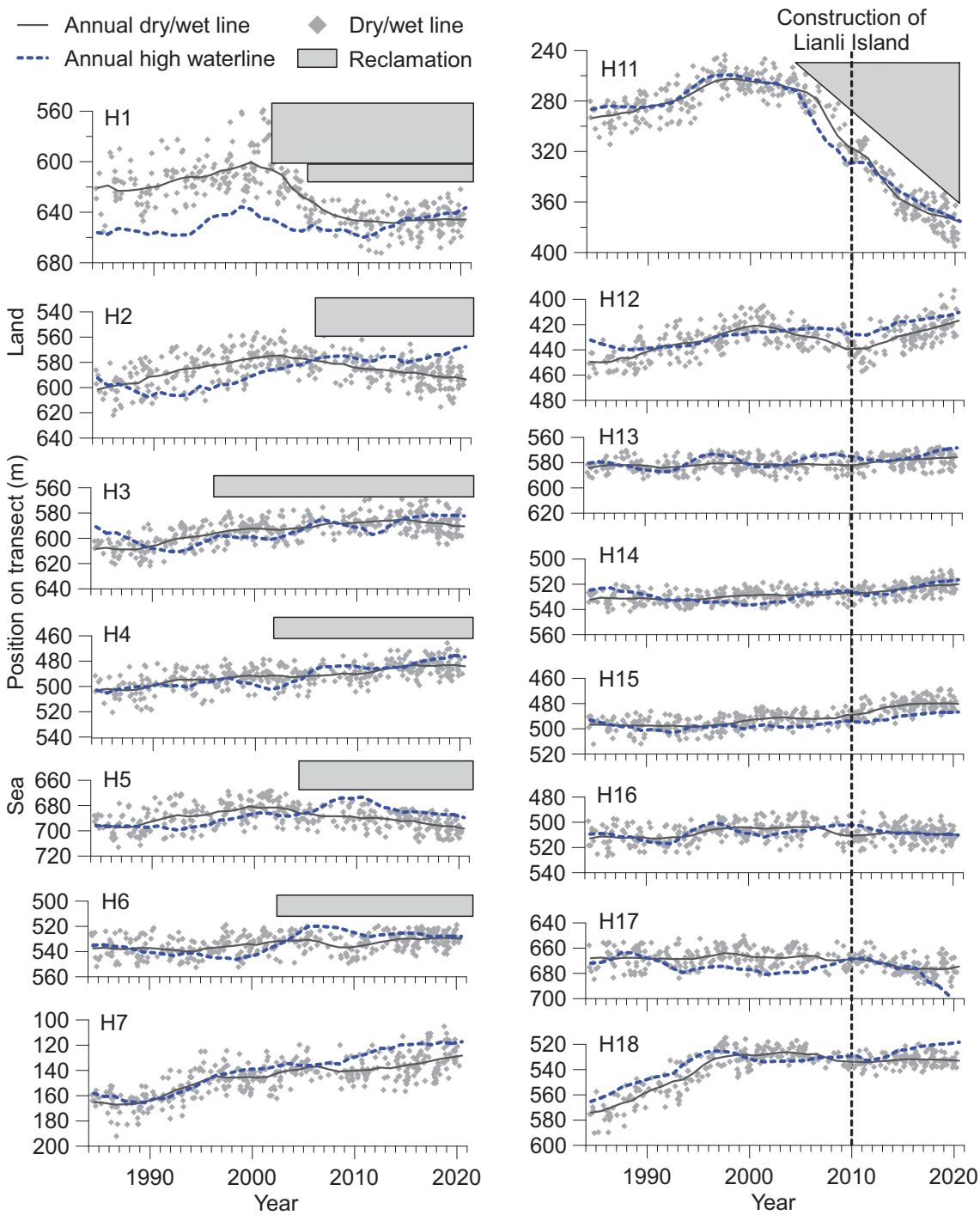

Fig. 8. Dry/wet line positions on transects H1–7 and H11–18 of Haiyang Beach.

Table 3
Error statistics of the dry/wet line positions on transects H1–7 and H11–18.

Transect	Number of images	Data acquired	Data acquisition ratio	Modified standard deviation (m)
H1	411	374	91%	13.6
H2	411	386	94%	9.8
H3	411	388	94%	7.4
H4	411	384	93%	7.1
H5	411	379	92%	7.8
H6	411	378	92%	6.9
H7	411	384	93%	9.3
H11	411	383	93%	9.8
H12	411	361	88%	8.8
H13	411	366	89%	5.4
H14	411	382	93%	4.9
H15	411	378	92%	5.4
H16	411	383	93%	6.9
H17	411	370	90%	7.0
H18	411	336	82%	6.8
Average	411	375	91%	7.8

checkpoints remain basically stable, and the average random error is 6.4 m, which is close to the results of Pardo-Pascual et al. (2018) and Vos et al. (2019) mentioned earlier. The above results indicate that CASPRS is capable of subpixel recognition of satellite images. The average data acquisition ratio of the checkpoints is 79%, which shows that the high-precision recognition results cannot be obtained in all cases.

4.3. Dry/wet line and waterline positions on the transects

Fig. 8 shows the dry/wet line positions on transects H1–7 and H11–18, and the error statistics results are listed in Table 3. The average data acquisition ratio of the dry/wet lines is 91% and greater than that of the checkpoints, which might be attributed to line features being easier to identify than point features. The average random error of the dry/wet line is 7.8 m and slightly great than that of the checkpoints.

Fig. 9 shows the waterline positions on H1–18, and the variation statistics results are shown in Table 4. The reason for using "variation statistics" rather than "error statistics" is that the variation of waterline positions is mainly caused by water level fluctuation rather than random error. The average data acquisition ratio is 75%, and the average of the modified standard deviation is 77.9 m.

4.4. Beach profile shapes and beach slopes

In addition to the waterline positions, the dry/wet line positions are also used to derive the beach profile shapes and beach slopes because the waterline position data above the mean high water are scarce (Fig. 10). Since the beach slopes are very small, their reciprocals are easier to display and understand. The best fit lines in Figs. 10 and 11 are based on group regression analysis method introduced earlier. The relationships between the shoreline positions and water levels show the characteristics of piecewise linear change, and the water levels of the inflection points are not fixed (Fig. 10-11).

For comparison, the entire beach profile was divided into supratidal, upper intertidal, lower intertidal, and subtidal zones, and the slope of each zone was calculated based on the predominant line of best fit in the zone. In some zones, such as the lower intertidal zone of H10, the two lines of best fit are basically the same length; therefore, the average of the reciprocals of the slopes is used in these zones. In general, the supratidal zone were steep (the reciprocals of the slopes are 4–26 with an average of 12) and stable. In the other zones, the slopes of H1–6 were medium (the reciprocals of the slopes are 75–143 with an average of 96) and stable, the slopes of H7–10 were relatively gentle (the reciprocals of the slopes are mainly 95–348 with an average of 216), and the slopes of H11–18 varied greatly in time and space (Fig. 10-12).

4.5. Erosion rates and intertidal widths

Using Eqs. 1–3 and the above results, the annual mean positions of the high-, mean-, and low-water lines were obtained (Fig. 9). The error analyses are shown in Tables 5-7. Since Haiyang Beach has undergone significant changes since 2010, the erosion rates during 1984–2010 and 2010–2020 and the intertidal widths in 1984, 2010, and 2020 were calculated (Fig. 13-14).

The changes in the dry/wet and high-water lines are similar (Figs. 6, 12), and their average difference is only 0.9 m (Table 8). According to the dry/wet and high-water lines and exclude the transects H1, H8–11 and H17–18 severely affected by onshore engineering projects and beach morphology as mentioned below, the Haiyang Beach was in a weakly eroded state, and the mean erosion rate of transects H2–7 and H12–16 was 0.55 m/year, and there is no obvious trend in temporal and spatial changes (Fig. 13A, B).

Compared with the dry/wet and high-water lines, the mean-water line is more dynamic and the low-water line has the highest dynamics (Fig. 13). According to the low-water line, the accretion of Haiyang Beach mainly occurred around the Dongcun River delta (H7–11) and the northern H17–18. The mean accretion rate of the transects H7–11 and H17–18 increased from early 1.07 m/year to later 2.92 m/year. The beaches by transects H1–6 and H12–16 transformed from early stable to later erosion. The mean erosion rate of transects H1–6 increased from early −0.31 m/year (negative number means accretion) to later 1.77 m/year while the mean erosion rate of transects H12–16 increased from early 0.23 m/year to later 3.72 m/year (Fig. 13C, D). The change of the mean-water line is similar to the low-water line, but the change is slow.

The intertidal widths of H1–6 and H11–16 are smaller than those of H7–10 and H17–18, and the intertidal widths of H1–6 and H11–15 gradually decrease from southwest to northeast (Fig. 14). In addition, the low boundary line of the waterline positions, which is used to show the shoreline change at the aforementioned low boundary water, was manually drawn in Fig. 9, and the slope of the low boundary line is its accretion/erosion rate.

5. Discussion

5.1. Setup of transects and recognition of dry/wet lines and waterlines on transects

The dry/wet line position is affected by lowlands, drainage ditches, and sand ridges (Fig. 2A, C, D and G). Therefore, the positions of the transects were designed to avoid the above objects as much as possible. However, the lowland around H1 and the sand ridges around H8–10 and H17 had large spatial ranges and could not be avoided. The early dry/wet line positions on H1 are actually the landside boundary of the lowland (Fig. 2C), and the dry/wet line positions on H8–10 were not identified owing to the sandy ridges, as shown before. By H17, although the dry sandy ridges are also scattered on the wet beach, there is an obvious dry/wet line on the upper beach. Therefore, the upper dry/wet lines were identified on H17 (Fig. 2G). Sometimes there are two strips of wet zones on the beach. In this case, the wet zone that is narrower than

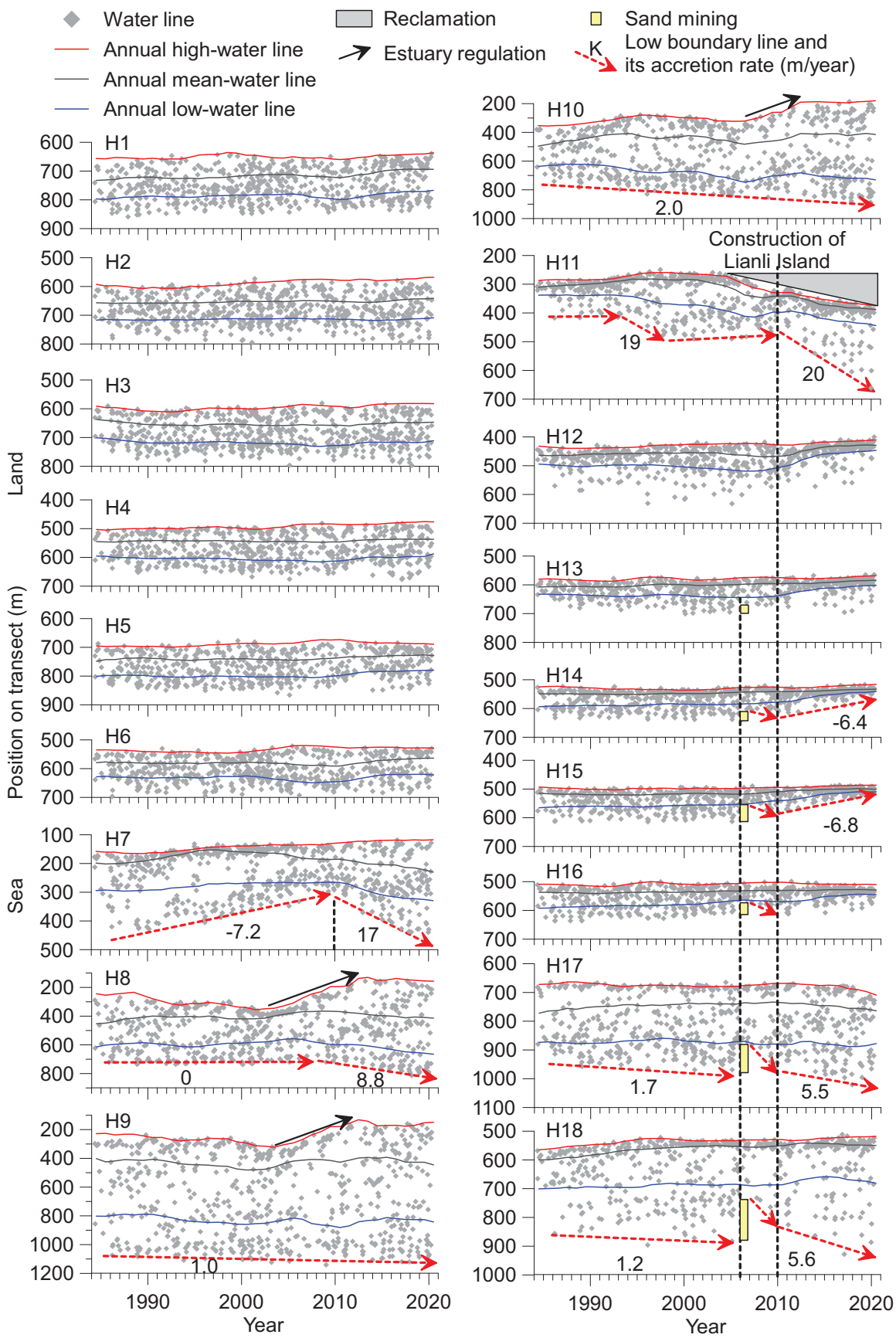

Fig. 9. Waterline positions on transects H1–18 of Haiyang Beach.

Table 4
Variation statistics of the waterline positions on transects H1–18.

Transect	Number of images	Data acquired	Data acquisition ratio	Modified standard deviation (m)
H1	880	674	77%	54.5
H2	880	668	76%	50.1
H3	880	685	78%	51.9
H4	880	654	74%	48.3
H5	880	622	71%	45.2
H6	880	620	70%	42.7
H7	880	696	79%	78.9
H8	880	685	78%	157.5
H9	880	688	78%	296.1
H10	880	678	77%	184.0
H11	880	714	81%	56.2
H12	880	666	76%	37.0
H13	880	626	71%	26.5
H14	880	716	81%	26.5
H15	880	643	73%	27.8
H16	880	663	75%	29.7
H17	880	650	74%	94.7
H18	880	586	67%	94.4
Average	880	663	75%	77.9

the dry zone on its sea side is ignored (Fig. 2C, F).

As shown before, when the water level was high, the Dongcun River delta was completely submerged, leaving only the funnel-shaped river mouth. At this time, the waterline positions did not exist on transects H8–10 (Fig. 2E). However, to study the influence of the estuary regulation project, the waterlines on the adjacent beaches were connected to form an imaginary waterline, and the positions of the imaginary waterline on H8–10 were manually identified (Fig. 2E).

The Haiyang Beach is not only composed of the above-mentioned geomorphic units, but is also affected by onshore and offshore engineering projects, as will be discussed below. Coupled with the influences of clouds, waves, highly turbid water, sensor noise, and sensor failure, it is unrealistic to study the evolution of complex beaches such as Haiyang Beach using only an automatic shoreline recognition algorithm.

5.2. Main factors affecting the evolution of Haiyang Beach

The evolution of Haiyang Beach is mainly attributed to onshore and offshore engineering projects, beach morphology, nearshore sediment transport, and river sediment reduction. The impacts of different engineering projects varied greatly. The onshore aquafarms by transect H1 enclosed the adjacent lowland (Fig. 2C, D), causing the dry/wet line to move 40 m toward the sea, but the high-water line derived from waterline was basically unaffected (Fig. 8). The onshore aquafarms at H2–6 did not enclose the beach and did not cause obvious changes to the shorelines (Fig. 8). However, the onshore engineering project near H11 encroached on the beach (Fig. 2E), causing the shorelines to move 100 m toward the sea (Fig. 8-9). The subsequent landward retreat of the high-water line at H8–10 might be attributed to the estuary regulation project of the Dongcun River mouth. In the project, the sand ridges on both sides of the river mouth were dredged (Fig. 9).

As mentioned earlier, the nearshore sediment is mainly transported to the northeast in the study area (Zhang et al., 2012; Ren et al., 2016). The sediment transported to the northeast will definitely be blocked by the protruding Dongcun River delta, contributing to the accretion of the beach at H7 in the middle and lower zones (Figs. 9, 11). In addition, the sediments discharged by Dongcun River into the sea could also exert a positive influence on the evolution of adjacent beach. The groin and jetty by H17–18 could also block the northeast transport of nearshore sediment, resulting in the accretion of adjacent beach (Fig. 13).

The construction of offshore Lianli Island and the bridge in 2010 might have two effects on the evolution of the beach. On the one hand, the construction weakened the hydrodynamic conditions nearby, causing the accelerated accretion of the mean-water line (accelerate at 3.8–6.9 m/year), low-water line (accelerate at 2.0–8.6 m/year), and low boundary line (accelerate at 8.8–24.2 m/year) on transects H7–8 and H11 (Figs. 9, 13). On the other hand, the construction could have hindered the transport of nearshore sediment to the northeast, causing the mean- and low-water lines on H12–16 to erode at a rate of 0.3–5.4 m/year. The erosion rates are twice that of the mean- and low-water lines on H2–6 during the same period (Fig. 13). The sediment in the adjacent water may have been gathered for the construction of Lianli Island, accelerating the erosion of adjacent beach.

The transformation of mean- and low-water lines on H1–6 from early stable to later erosion at a rate of 0.5–3.2 m/year (Fig. 13) should be attributed to the sediment reduction in the surrounding rivers, as there is no offshore engineering project upstream (southwest) of H1–6 on the sediment transport path. The sudden constriction of the subtidal zones at H13–18 in 2006 should be the aftermath of the offshore sand mining for the construction of onshore sand sculptures (Fig. 1, 2F, 9).

Incidentally, although the potential causes of the morphological change in the study area are mainly the onshore and offshore engineering projects, further investigation using more quantitative field survey data is needed to confirm this.

5.3. Position errors of the checkpoints and shorelines and their main influencing factors

The random error of the checkpoints can be considered as resulting mainly from the registration process of the satellite images since its average, which is 6.4 m, is equivalent to the geo-reference error, which is 0–12 m, as shown before. The random errors of the dry/wet, high-water, mean-water, and low-water lines are summarized in Table 9. Since the dry/wet line has no data on H8–10, the data of the other three shoreline indicators were recalculated based on the data of H1–7 and H11–18. The averages of the random errors of the dry/wet, high-water, mean-water, and low-water lines are 7.8 m, 10.5 m, 15.9 m, and 19.2 m, respectively, which are higher than that of the checkpoint.

Previous studies have shown that beach slope or beach width will affect the position error of shorelines (Almonacid-Caballer et al., 2016; Hagenaars et al., 2018; Zhang et al., 2018a). This paper further analyzed the relationship between the random errors and beach slopes (Fig. 15). The result shows that the fitting function between the random errors and the reciprocals of the beach slopes is a quadratic function. The vertical intercept of the quadratic function is 8.8 m, which means that the random error of the shoreline on the steepest beach is roughly equivalent to the random errors of the checkpoint and dry/wet line. With an increase in the reciprocal of the slope, the random error increases faster. This may be because the impact of beach undulations is relatively large on flat beaches.

Although the shoreline error is intuitively related to the beach slope, it originates from many physical processes, mainly tides and waves, and is associated with the error between the simulated water level and the actual water level. The beach profile transforms the vertical water level errors into the horizontal shoreline errors. Except for water level errors, irregular undulations of beach profiles will also introduce errors to the

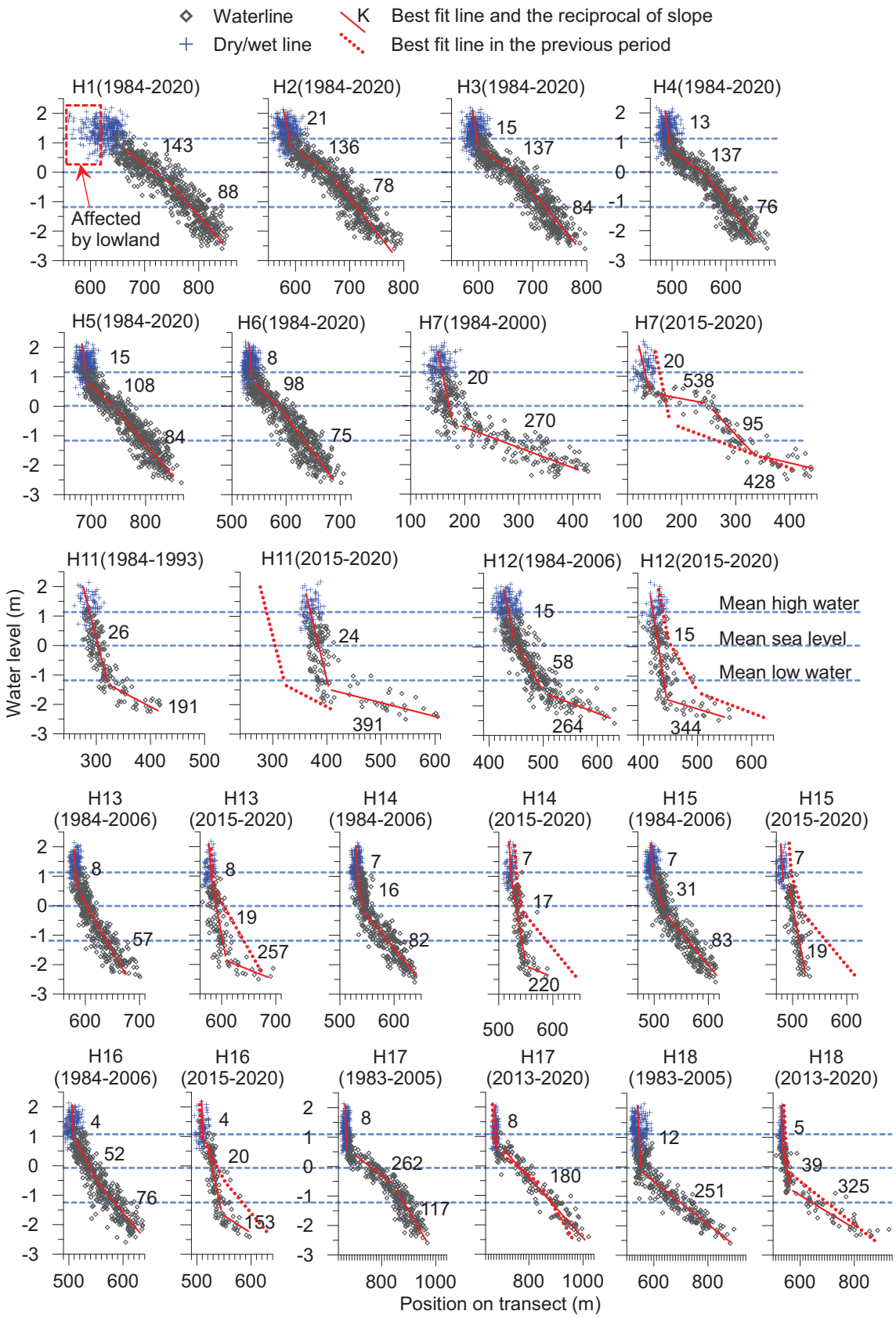

Fig. 10. Profile shapes and slopes of Haiyang Beach on transects H1–7 and H11–18 in different time periods.

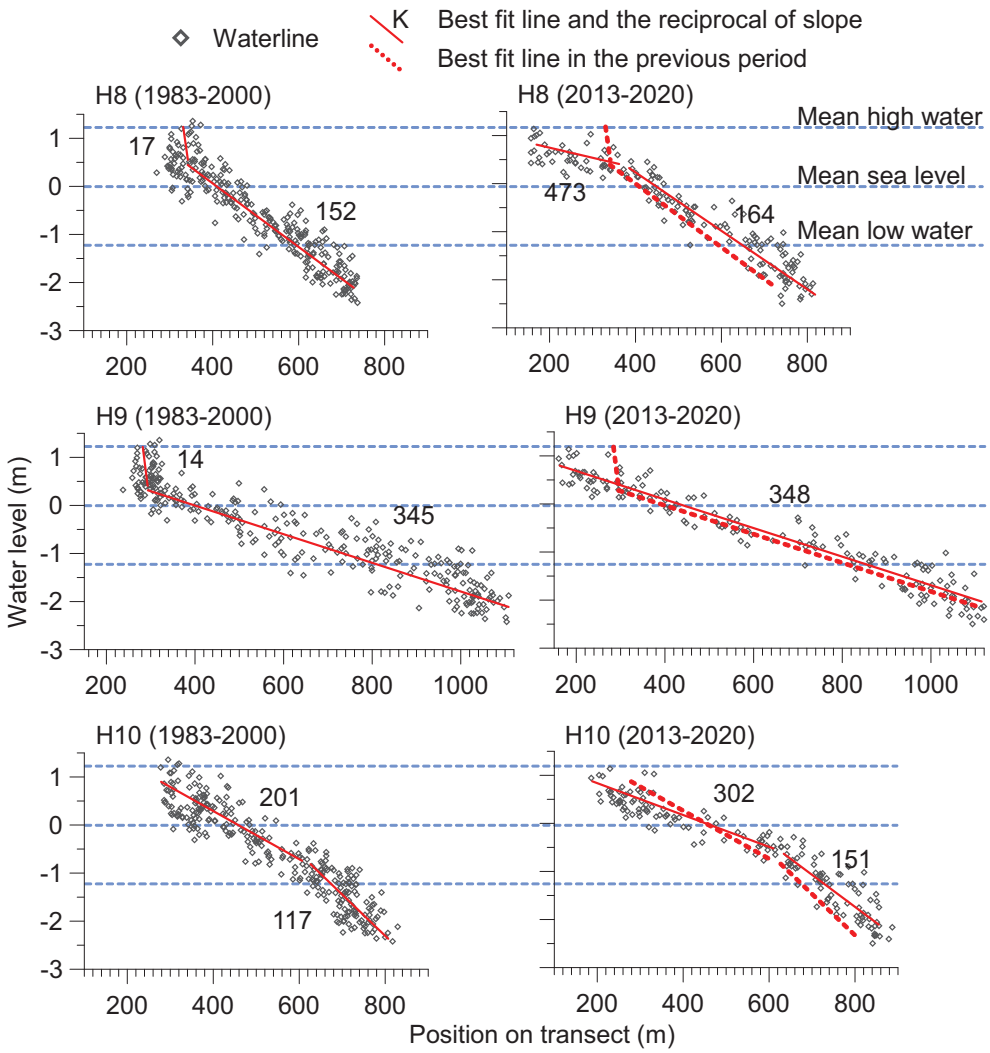

Fig. 11. Profile shapes and slopes of Haiyang Beach on transects H8–10 in different time periods.

shoreline since the current water level correction method assumes that the beach profile changes linearly (Eqs. 1–3).

5.4. Comparison of shoreline indicators

In terms of random error, the dry/wet line has the smallest error, followed by the high-, mean-, and low-water lines. The variation range of waterline vary from 42.7–296.1 m, which is relatively large. Water level correction must be performed before using waterline to study beach evolution. The random errors of the high-, mean-, and low-water lines vary from 6.5–94.9 m, which depends on the beach slopes of their corresponding zones that vary from 1:4–1:391 as shown in Fig. 10-12.

In terms of data acquisition ratio, the ratios of the dry/wet line and waterline are high, the ratios of the low- and mean-water lines are medium, and the ratio of the high-water line is low. It should be noted that the average acquisition ratio of the waterline on the 411 good-quality images is 90%, which is equivalent to the ratio of the dry/wet line. If the high-, mean-, and low-water lines are extracted from the 411 good-quality images, the data acquisition ratio will also increase by approximately 1.2 times. The low acquisition ratio of the high-water line is due to the high water levels are rare when the Landsat images were taken, as shown before. The low data acquisition ratio of the high-water line is not conducive to the use of statistical methods to further improve the accuracy of beach evolution studies.

In terms of physical meaning, the dry/wet line may not indicate a change in the high-water line since it can be affected by drainage ditches and beach topography. For example, before the lowland around H1 was enclosed, the dry/wet line deviated greatly from the high-water line (Fig. 2C, 8). The dry/wet lines, which are affected by drainage ditches and beach topography, should be used in conjunction with the high-water lines, which have a low data acquisition ratio, in beach evolution studies to compensate for the above shortcomings. Changes in the dry/wet and high-water lines are directly affected by onshore engineering but are less affected by offshore engineering. Different from the dry/wet and high-water lines, changes in the mean- and low-water lines are mainly controlled by the nearshore transport of sediment; therefore, they are more affected by offshore engineering. The low boundary line is the outermost shoreline that can be derived from Landsat images and is more sensitive to the nearshore transport of sediment and the impact of offshore engineering than the other indicators.

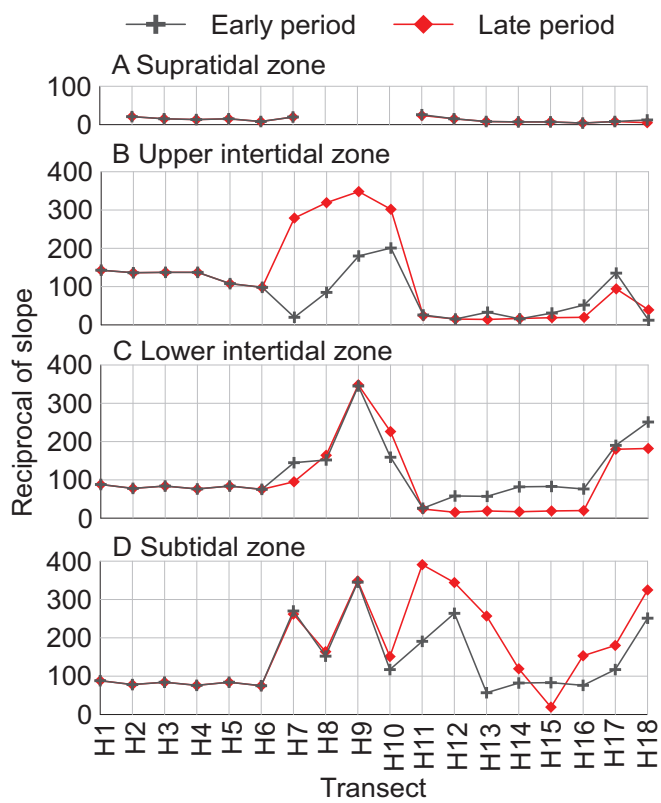

Fig. 12. Early and late slopes of the supratidal (A), upper intertidal (B), lower intertidal (C), and subtidal (D) zones of Haiyang Beach on transects H1–18.

Table 5
Error statistics of the high-water line positions on transects H1–18.

Transect	Number of images	Data acquired	Data acquisition ratio	Modified standard deviation (m)
H1	880	147	17%	15.0
H2	880	151	17%	15.2
H3	880	159	18%	12.1
H4	880	146	17%	12.0
H5	880	135	15%	9.5
H6	880	142	16%	9.3
H7	880	150	17%	8.8
H8	880	155	18%	48.3
H9	880	153	17%	38.8
H10	880	154	18%	35.3
H11	880	175	20%	14.8
H12	880	151	17%	9.8
H13	880	145	16%	7.6
H14	880	166	19%	6.5
H15	880	140	16%	7.1
H16	880	159	18%	7.6
H17	880	150	17%	13.2
H18	880	152	17%	8.7
Average	880	152	17%	15.5

6. Conclusions

This paper provides a novel and practical software and method for studying the beach evolution using as many free medium-resolution satellite images as possible. This method combines subpixel and human-computer interaction technologies, and focuses on transects, and uses dry/wet line and waterline to comprehensively study beach evolution. The use of subpixel technology makes up for the low resolution of historical satellite images. The use of human-computer interaction technology ensures that the recognition results are correct even if the

Table 6
Error statistics of the mean-water line positions on transects H1–18.

Transect	Number of images	Data acquired	Data acquisition ratio	Modified standard deviation (m)
H1	880	345	39%	20.1
H2	880	331	38%	17.0
H3	880	330	38%	17.3
H4	880	313	36%	14.8
H5	880	304	35%	13.6
H6	880	302	34%	14.6
H7	880	353	40%	24.7
H8	880	321	36%	45.3
H9	880	318	36%	81.7
H10	880	330	38%	51.3
H11	880	369	42%	20.1
H12	880	335	38%	13.6
H13	880	320	36%	8.9
H14	880	352	40%	8.1
H15	880	318	36%	8.9
H16	880	328	37%	8.5
H17	880	320	36%	27.2
H18	880	296	34%	20.6
Average	880	327	37%	23.1

Table 7
Error statistics of the low-water line positions on transects H1–18.

Transect	Number of images	Data acquired	Data acquisition ratio	Modified standard deviation (m)
H1	880	431	49%	18.8
H2	880	417	47%	15.6
H3	880	428	49%	16.1
H4	880	420	48%	15.2
H5	880	404	46%	14.2
H6	880	406	46%	15.6
H7	880	438	50%	30.1
H8	880	438	50%	45.0
H9	880	437	50%	94.9
H10	880	434	49%	53.7
H11	880	453	51%	31.5
H12	880	433	49%	22.8
H13	880	405	46%	14.5
H14	880	470	53%	12.7
H15	880	431	49%	12.3
H16	880	424	48%	12.8
H17	880	405	46%	24.4
H18	880	350	40%	31.2
Average	880	424	48%	26.7

images are affected by clouds, beach morphology, and engineering projects. The focus on transects avoids the large workloads associating with identifying and correcting the entire shorelines, makes it practical to interpreting as many satellite images as possible. Comprehensive utilization of dry/wet line and waterline and the interpretation of hundreds of satellite images makes it possible to analyze the entire beach profile shape and further derive the high-, mean-, and low-water lines through tidal correction. The use of multiple shoreline indicators that complement and confirm each other helps to achieve a comprehensive understanding of the temporal and spatial evolution of the entire beach. In summary, the CARPRS software and the method are suitable for a comprehensive and detailed study of beach evolution using as many satellite images as possible.

The random errors of the checkpoints and dry/wet lines are 6.4 m and 7.8 m, respectively, which are comparable to the current cutting-edge studies using subpixel technology. The random errors of the high-, mean-, and low-water lines are 10.5 m, 15.9 m, and 19.2 m, respectively. The large errors of the high-, mean-, and low-water lines are mainly attributed to the gentle slope of Haiyang Beach which vary from 1:20–1:348 with an average of 1:124. The random errors are mainly affected by random water level fluctuations due to waves and

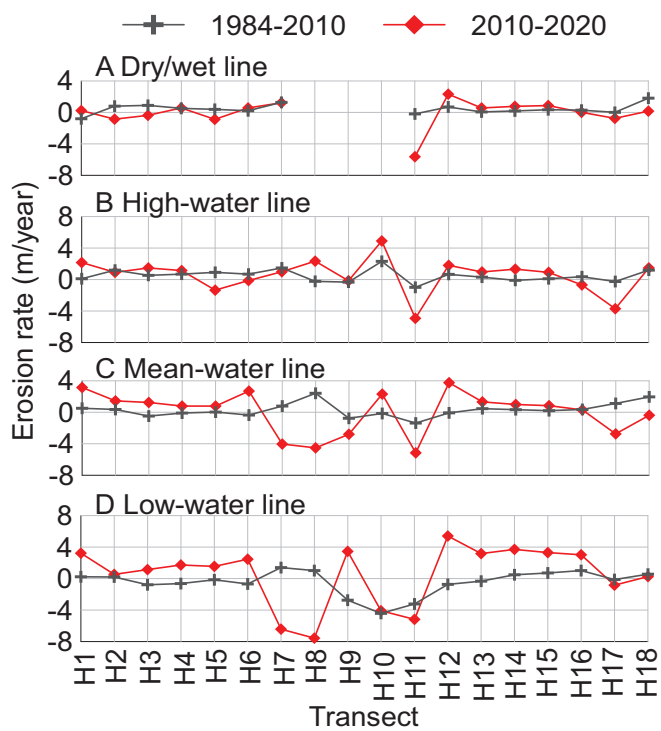

Fig. 13. Erosion rates of the dry/wet (A), high-water (B), mean-water (C), and low-water (D) lines on transects H1–18 of Haiyang Beach.

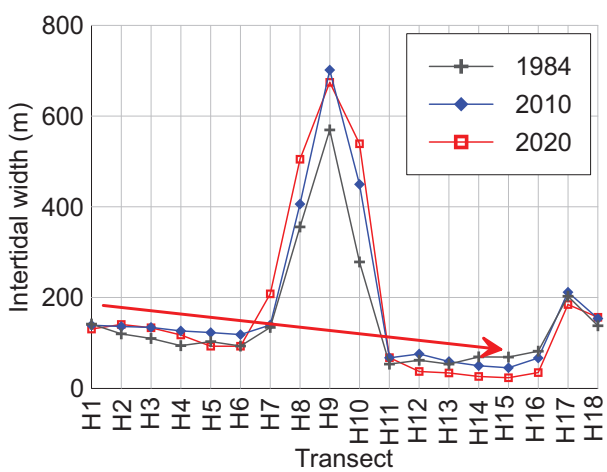

Fig. 14. Intertidal widths of Haiyang Beach on transects H1–18.

tides and irregular undulations of the beach profile shape. Although the errors of the shoreline indicators used in this paper have been greatly reduced, they are still relatively large, therefore, this paper recommends using hundreds of satellite images and statistical methods to study the evolution of beaches.

In theory, the waterline moves on the entire beach and can be used to study the evolution of the entire beach. However, due to the limitation of the shooting time, the Landsat satellite imagery lacks images at high water levels in the study area, resulting in the waterline positions identified from the Landsat images not being used to study the upper beach profile shape. The dry/wet line moves mainly on the upper beach, and it not only has a high data extraction ratio but also has a small error. Therefore, the dry/wet line unaffected by drainage ditches and beach topography can be used to study beach changes in the supratidal zone,

Table 8
Differences between the annual mean positions of the high-water and dry/wet lines on the transects.

Transect	Number of data	Average of difference (m)
H1	37	22.6
H2	37	1.5
H3	37	0.4
H4	37	−0.1
H5	37	−1.5
H6	37	−1.2
H7	37	−6.2
H11	37	0.2
H12	37	−5.1
H13	37	−2.5
H14	37	−0.1
H15	37	4.5
H16	37	−0.3
H17	37	6.7
H18	37	−5.2
Average	37	0.9

Table 9
Error statistics of the positions of dry/wet, high-water, mean-water, and low-water lines on transects H1–7 and H11–18.

Shoreline indicator	Number of images	Data acquired	Data acquisition ratio	Modified standard deviation (m)
Dry/wet line	411	375	91%	7.8
High-water line	880	151	17%	10.5
Mean-water line	880	328	37%	15.9
Low-water line	880	421	48%	19.2

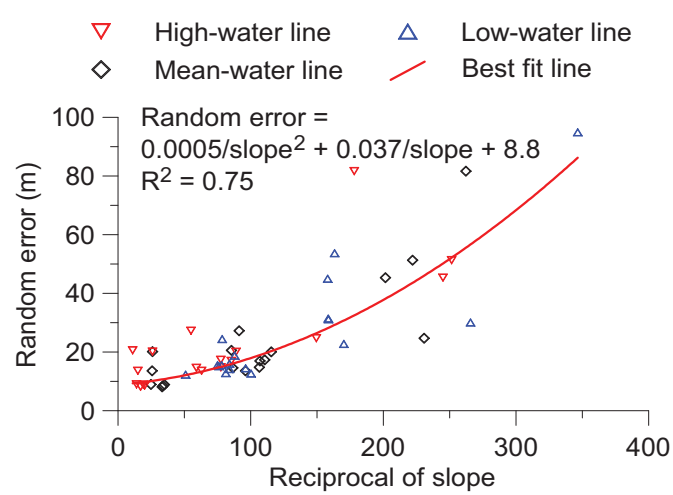

Fig. 15. Relationship between the beach slopes and the random errors of high-, mean-, and low-water lines.

and it is a useful supplement to the waterline indicator. The dry/wet and high-water lines are mainly affected by onshore engineering, while the mean-water, low-water and low boundary lines are mainly affected by nearshore transport of sediment and offshore engineering.

Data availability

The software and data can be found at https://github.com/ouczxd/CASPRS. The satellite images can be also downloaded from http://glovis.usgs.gov.

Declaration of Competing Interest

The authors declare that they have no known competing financial interests or personal relationships that could have appeared to influence the work reported in this paper.

Acknowledgments

This work was supported by the Shandong Provincial Natural Science Foundation, China (ZR2019MD037), the Fundamental Research Funds for the Central Universities (202072003), and the National Natural Science Foundation of China (41776059). We are greatly indebted to the Editor-in-Chief Edward Anthony and three anonymous reviewers for their constructive comments and valuable suggestions.

References

Alexandrakis, G., Manasakis, C., Kampanis, N.A., 2015. Valuating the effects of beach erosion to tourism revenue A management perspective. Ocean Coast. Manag. 111, 1–11.
Almonacid-Caballer, J., Sánchez-García, E., Pardo-Pascual, J.E., Balaguer-Beser, A.A., Palomar-Vázquez, J., 2016. Evaluation of annual mean shoreline position deduced from Landsat imagery as a mid-term coastal evolution indicator. Mar. Geol. 372, 79–88.
Anthony, E.J., 2015. Wave influence in the construction, shaping and destruction of river deltas: a review. Mar. Geol. 361, 53–78. https://doi.org/10.1016/j.margeo.2014.12.004.
Ballesteros, C., Jiménez, J.A., Valdemoro, H.I., Bosom, E., 2018. Erosion consequences on beach functions along the Maresme coast (NW Mediterranean, Spain). Nat. Hazards 90 (1), 173–195, 2018.
Bird, E.C.F., 1985. Coastline Changes; a Global Review. Wiley, Chichester.
Boak, E.H., Turner, I.L., 2005. Shoreline Definition and Detection: a Review. J. Coast. Res. 214, 688–703.
Brooks, S., 2020. Disappearing beaches. Nat. Clim. Chang. 10, 188–190.
Brown, S., Nicholls, R.J., 2015. Subsidence and human influences in mega deltas: the case of the Ganges–Brahmaputra–Meghna. Sci. Total Environ. 527-528, 362–374.
Burt, J.A., Bartholomew, A., 2019. Towards more sustainable coastal development in the Arabian Gulf: Opportunities for ecological engineering in an urbanized seascape. Mar. Pollut. Bull. 142, 93–102.
Burvingt, O., Masselink, G., Russell, P., et al., 2017. Classification of beach response to extreme storms. Geomorphology 295.
Cai, F., Su, X., Liu, J., Li, B., Lei, G., 2009. Coastal erosion in China under the condition of global climate change and measures for its prevention. Prog. Nat. Sci. 19, 415–426.
Cazenave, A., Cozannet, G.L., 2014. Sea level rise and its coastal impacts. Earths Future 2 (2), 15–34.
Cooper, J.A.G., Masselink, G., Coco, G., Short, A.D., Castelle, B., Rogers, K., Anthony, E., Green, A.N., Kelley, J.T., Pilkey, O.H., Jackson, D.W.T., 2020. Sandy beaches can survive sea-level rise. Nat. Clim. Chang. 10, 993–995. https://doi.org/10.1038/s41558-020-0697-0.
Couvillion, B.R., Barras, J.A., Steyer, G.D., Sleavin, W., Fischer, M., Beck, H., et al., 2011. Land Area Change in Coastal Louisiana from 1932 to 2010. U.S. Geological Survey Scientific Investigations Map, p. 3164 (scale 1:265,000).
Editorial Board of China Bay Survey, 1993. Survey of China Bays, vol. 4. China Ocean Press, Beijing (In Chinese).
García-Rubio, G., Huntley, D., Russell, P., 2015. Evaluating shoreline identification using optical satellite images. Mar. Geol. 359, 96–105.
Hagenaars, G., Vries, S.D., Luijendijk, A.P., et al., 2018. On the accuracy of automated shoreline detection derived from satellite imagery: a case study of the sand motor mega-scale nourishment. Coast. Eng. 133, 113–125.
Jackson, N.L., Nordstrom, K.F., 2020. Trends in research on beaches and dunes on sandy shores, 1969–2019. Geomorphology 366, 106737.
Li, Y.X., Yand, G.H., Yang, S.D., et al., 2001. Preliminary division of active block boundary in Chinese mainland based on recent vertical crustal movement. Acta Seismol. Sin. 23 (1), 11–16 (In Chinese with English abstract).
Li, G.X., Gong, L.X., Yang, J.C., Ding, D., Li, B., Cao, L.H., Wang, Y.H., Liu, L., 2013. Beach erosion along the coast of Shandong Province and protection countermeasures. Mar. Geol. Quat. Geol. 33 (5), 35–46 (In Chinese with English abstract).
López, I., López, M., Aragonés, L., et al., 2016. The erosion of the beaches on the coast of Alicante: study of the mechanisms of weathering by accelerated laboratory tests. Sci. Total Environ. 566-567, 191–204.
Ludka, B.C., Guza, R.T., O'Reilly, W.C., et al., 2019. Sixteen years of bathymetry and waves at San Diego beaches. Scientific Data 6, 161. https://doi.org/10.1038/s41597-019-0167-6.
Luijendijk, A., Hagenaars, G., Ranasinghe, R., et al., 2018. The State of the World's Beaches. Sci. Rep. 8, 6641. https://doi.org/10.1038/s41598-018-24630-6.
Maiti, S., Bhattacharya, A.K., 2009. Shoreline change analysis and its application to prediction: a remote sensing and statistics based approach. Mar. Geol. 257 (1), 11–23.
Matsumoto, K., Takanezawa, T., Ooe, M., 2000. Ocean tide model developed by assimilating TOPEX/POSEIDON altimetry data into hydrodynamical model: a global and a regional model around Japan. J. Oceanogr. 56, 567–581.
Mentaschi, L., Vousdoukas, M.I., Pekel, J., Voukouvalas, E., Feyen, L., 2018. Global long-term observations of coastal erosion and accretion. Sci. Rep. 8, 12876.
Nicholls, R.J., Cazenave, A., 2010. Sea-level rise and its impact on coastal zones. Science 328 (5985), 1517–1520.
Pagán, J., Aragonés, L., Tenza-Abril, A., Pallarés, P., 2016. The influence of anthropic actions on the evolution of an urban beach: Case study of Marineta Cassiana beach, Spain. Sci. Total Environ. 559, 242–255.
Pagán, J., López, I., Aragonés, L., Garcia-Barba, J., 2017. The effects of the anthropic actions on the sandy beaches of Guardamar del Segura, Spain. Sci. Total Environ. 1364–1377 s601–602.
Pagán, J., López, M., López, I., Aragonés, L., 2018. Causes of the different behaviour of the shoreline on beaches with similar characteristics. Study case of the San Juan and Guardamar del Segura beaches, Spain. Sci. Total Environ. 634, 739–748.
Pardo-Pascual, J., Almonacid-Caballer, J., Ruiz, L., Palomar-Vázquez, J., 2012. Automatic extraction of shorelines from Landsat TM and ETM+ multi-temporal images with subpixel precision. Remote Sens. Environ. 123 (6), 1–11.
Pardo-Pascual, J.E., Sánchez-García, E., Almonacid-Caballer, J., Palomar-Vázquez, J.M., Santos, E.P.D.L., Fernández-Sarría, A., Balaguer-Beser, Á., 2018. Assessing the accuracy of automatically extracted shorelines on microtidal beaches from Landsat 7, Landsat 8 and Sentinel-2 imagery. Remote Sens. 10, 326.
Ranasinghe, R., 2016. Assessing climate change impacts on open sandy coasts: a review. Earth Sci. Rev. 160.
Ren, Z.H., Hu, R.J., Zhang, L.J., Wang, N., Zhu, L.H., 2016. Evolution of the sandy beach in Haiyang. Marine Geol. Front. 32 (11), 19–25 (In Chinese with English abstract).
Romine, B.M., Fletcher, C.H., 2013. A summary of historical shoreline changes on beaches of Kauai, Oahu, and Maui; Hawaii. J. Coast. Res. 29 (3), 605–614.
Rouse, L.J., Roberts, H.H., Cunningham, R.H.W., 1978. Satellite observation of the subaerial growth of the Atchafalaya Delta, Louisiana. Geology 6 (7), 405.
Ryu, J.H., Won, J.S., Min, K.D., 2002. Waterline extraction from Landsat TM data in a tidal flat a case study in Gomso Bay, Korea. Remote Sens. Environ. 83 (3), 442–456.
Segura, L.E., Hansen, J.E., Lowe, R.J., Symonds, G., Contardo, S., 2018. Shoreline variability at a low-energy beach: Contributions of storms, megacusps and sea-breeze cycles. Mar. Geol. 400, 94–106.
Thieler, E.R., Himmelstoss, E.A., Zichichi, J.L., Ergun, A., 2009. Digital Shoreline Analysis System (DSAS) version 4.0: an ArcGIS extension for calculating shoreline change. In: US Geological Survey Open File Report (2008–1278).
Turner, I.L., Harley, M.D., Short, A.D., Simmons, J.A., Bracs, M.A., Phillips, M.S., et al., 2016. A multi-decade dataset of monthly beach profile surveys and inshore wave forcing at Narrabeen. Australia. Sci. Data 3, 160024.
Vos, K., Harley, M.D., Splinter, K.D., Simmons, J.A., Turner, I.L., 2019. Sub-annual to multi-decadal shoreline variability from publicly available satellite imagery. Coast. Eng. 150, 160–174.
Vos, K., Harley, M.D., Splinter, K.D., Walker, A., Turner, I.L., 2020. Beach slopes from satellite-derived shorelines. Geophys. Res. Lett. 47 (e2020GL088365.
Vousdoukas, M.I., Ranasinghe, R., Mentaschi, L., 2020a. Sandy coastlines under threat of erosion. Nat. Clim. Chang. 10, 260–263. https://doi.org/10.1038/s41558-020-0697-0.
Vousdoukas, M.I., Ranasinghe, R., Mentaschi, L., Plomaritis, T.A., Athanasiou, P., Luijendijk, A., Feyen, L., 2020b. Reply to: Sandy beaches can survive sea-level rise. Nat. Clim. Chang. 10, 996–997. https://doi.org/10.1038/s41558-020-00934-2.
Webb, A.P., Kench, P.S., 2010. The dynamic response of reef islands to sea-level rise: evidence from multi-decadal analysis of island change in the Central Pacific. Glob. Planet. Chang. 72, 234–246.
Wenneker, I., Spelt, B., Peters, H., Ronde, J.D., 2016. Overview of 20 years of field measurements in the coastal zone and at the Petten Sea dike in the Netherlands. Coast. Eng. 109, 96–113.
Xia, D.X., Wang, W.H., Wu, G.Q., Cui, J.R., Li, F.L., 1993. Coastal erosion in China. Acta Geograph. Sin. 48 (5), 468–476 (In Chinese with English abstract).
You, Z.J., Ji, Z.Y., Bai, Y.C., 2018. Impacts of storm wave-induced coastal hazards on the coast of China. J. Coastal Res. SI 85, 826–830.
Zhang, Y.H., Wu, J.Z., Zhu, L.H., Hu, R.J., Sun, Y.G., 2012. Impacts of the construction of the east wing of Haiyang harbor of the erosion and deposition regime in the sandy coast. Marine Geology Frontiers. 28 (8), 49–55 (In Chinese with English abstract).
Zhang, X.D., Yang, Z.S., Zhang, Y.X., Ji, Y., Wang, H.M., Lv, K., Lu, Z.Y., 2018a. Spatial and temporal shoreline changes of the southern Yellow River (Huanghe) Delta in 1976–2016. Mar. Geol. 395, 188–197.
Zhang, X.D., Lu, Z.Y., Jiang, S.H., Chi, W.Q., Zhu, L.H., Wang, H.M., Lv, K., Wang, B.Y., Yang, Z.S., 2018b. The progradation and retrogradation of two newborn Huanghe (Yellow River) Delta lobes and its influencing factors. Mar. Geol. 400, 38–48.
Zhang, X.D., Zhang, Y.X., Zhu, L.H., Chi, W.Q., Yang, Z.S., Wang, B.Y., Lv, K., Wang, H. M., Lu, Z.Y., 2018c. Spatial-temporal evolution of the eastern Nanhui mudflat in the Changjiang (Yangtze River) Estuary under intensified human activities. Geomorphology 309, 38–50.
Zhang, R., Chen, L.H., Liu, S.S., et al., 2019. Shoreline evolution in an embayed beach adjacent to tidal inlet: the impact of anthropogenic activities. Geomorphology 346, 106856.
Zhang, X., Fan, D., Yang, Z., Xu, S., Chi, W., Wang, H., 2020. Sustained growth of river mouth bars in the vulnerable Changjiang Delta. J. Hydrol. 590, 125450.
Zhuang, Z.Y., Chen, W.M., Xu, W.D., Shen, C.L., 1989. Retrogression of straight sandy beaches in the Shandong peninsula and its results. J. Ocean University Qingdao 19 (1), 90–98 (In Chinese with English abstract).